Correspondence to:
A. Agarwal,
amar@daad-alumni.de

Impact Experiment on Gneiss: The Effects of Foliation on Cratering Process

Amar Agarwal[1,2], Michael H. Poelchau[1], Thomas Kenkmann[1], Auriol Rae[1], and Matthias Ebert[1]

[1]Department of Geology, University of Freiburg, Freiburg, Germany, [2]Department of Earth Sciences, Indian Institute of Technology-Kanpur, Kanpur, India

Abstract Two impact experiments were carried out on blocks of Maggia gneiss to assess the influence of mechanical target anisotropies on the cratering process. The experiments were done within the framework of Multidisciplinary Experimental and Modeling Impact Research Network. In one experiment the metamorphic foliation was vertical, that is, oriented perpendicular to the target surface, and in the other horizontal, that is, parallel to the target surface. This study reveals that due to preferred spallation along the foliation, the cratering efficiency is higher if the foliation is horizontal. The study further presents a comprehensive quantitative strain analysis in the subsurface of these craters. We use biotite kink bands as strain markers. The distribution of strain differs strongly in both experiments. If the foliation is vertical, the area beneath the central crater floor shows a high compressive strain. This is attributed to the ability of biotite to kink more easily when shortened parallel to its basal plane. If the foliation is horizontal, surface kinking is reduced and tensile failure along the foliation deepens the crater during unloading.

1. Introduction

The surfaces of all solid planetary bodies have been intensely cratered, underlining the critical role of hypervelocity impact in their evolution. Impact craters, such as those on Earth, the Moon, Mars, and Venus, are either simple or complex craters with circular to polygonal outlines. Different crater sizes are primarily a function of impact energy and secondly of target strength properties and the impact angle (e.g., Cintala et al., 1977; Grieve et al., 1981; Melosh, 1989; Melosh & Ivanov, 1999; Osinski & Pierazzo, 2012; Pierazzo & Melosh, 2000; Pike, 1980; Poelchau et al., 2009; Wood et al., 1978). Here we consider the effect of anisotropic strength properties due to layering on the cratering process.

Most rocks display mechanical anisotropies and heterogeneities such as vertical/horizontal changes in density, and strength. These variations can significantly influence crater formation (e.g., Baud et al., 2005). The most remarkable vertical heterogeneity in target properties results from stratigraphic layering such as the transition from unconsolidated to consolidated sedimentary rock and from sedimentary rock to competent crystalline basement rocks (e.g., Pohl et al., 1977). Differences in thickness of the stratigraphic layering yield significant structural differences between terrestrial craters formed under similar conditions (Collins et al., 2008a; Stickle & Schultz, 2013; Hopkins et al., 2019), for example, larger transient and final crater diameters with a thicker sedimentary layer. Target layering is common on most bodies in the solar system (e.g., Senft & Stewart, 2007).

Quaide and Oberbeck (1968) experimentally investigated in small scale the effects of the weaker layer (loose, granular, noncohesive materials) lying over a stronger cohesive substrate to obtain insights into the formation of small craters on the Moon. They show that with a sufficient strength contrast, the stronger underlying layer affects the crater morphology when the crater diameter is at least 4 times the thickness of the layers. This may produce craters with flat floors or small deep craters nested within a shallow outer crater. Similar morphologies are observed in terrestrial craters formed in shallow-marine environments such as Chesapeake Bay (Gohn et al., 2008) or Lockne (Ormö & Lindström, 2000). On a much smaller scale, the shock wave reflects, refracts, and superposes at boundaries of materials with contrasting mechanical properties to cause localized intense shock deformation (e.g., Agarwal et al., 2016; Agarwal et al., 2016; Kenkmann et al., 2000).

Asymmetries in the crater planform causing polygonal crater shapes may result from lateral heterogeneities in the target, such as topography, tilted stratigraphy, faults, fractures, and joints (e.g., Eppler et al., 1983;

Öhman et al., 2010; Poelchau et al., 2009). To summarize, the rheological stratification of target rocks influences the overall deformation in the crater subsurface and the distribution of major impact-induced shear zones. The strain is often concentrated into weaker beds that govern further deformation.

To study the effect of layered targets with mechanical anisotropies on the cratering process and considering the required upscaling from experiment to nature, we selected a finely foliated gneiss for our study. This rock is particularly suitable for the study because it contains abundant micas, which record strain within kink bands.

Measurement of strain in deformed geological material is a well-established tool in geology to investigate microscale to regional-scale deformation (e.g., Joshi et al., 2017; Lisle, 1985; Ramsay & Huber, 1983). Determination of strain relies on calculating the length changes and angular distortions provided by the strain markers (Ramsay & Huber, 1983). A previous study of the experimental impact on a gneissic target revealed kinked biotites in the crater subsurface (Agarwal et al., 2019), which can be analyzed to quantify the compressive strain. Biotite is an important rock-forming mineral abundant in target rocks of many natural impact craters, such as Araguainha in Brazil, Botsumwi in Ghana, Chesapeake Bay, in the United States, Chicxulub in Mexico, Lockne in Sweden, Ries in Germany, Sudbury in Canada, and Vredefort in South Africa (e.g., Agarwal et al., 2015; Gohn et al., 2008; Kring et al., 2004; Riller, 2005; Schneider, 1972; Schreyer, 1983; Yokoyama et al., 2012).

Kinking of biotite is reported from natural and experimental impact craters at shock pressures ≥0.9 GPa (e.g., Agarwal et al., 2019; Chao, 1967; Cummings, 1965; Dressler, 1990; Gibson & Reimold, 2005; Hörz & Ahrens, 1969; Ogilvie et al., 2011; Schneider, 1972). Kinking in biotite depends on the shock pressure and on the orientation of (001) with respect to the shock front (Agarwal et al., 2019; Cummings, 1968; Ogilvie et al., 2011; Schneider, 1972). Kinking is mechanically accommodated by various gliding processes exclusively in the cleavage plane (001) due to the combination of peak pressures and the large accompanying dynamic strain, such that the rotation axes are confined to the {001} plane (Hörz, 1970; Hörz & Ahrens, 1969; Schneider, 1972). In general, the shock-generated kink bands are less symmetrical than kinks of static origin (Hörz, 1970; Hörz & Ahrens, 1969).

The present study aims to investigate the effect of layered target rocks on the cratering processes. Two blocks of Maggia gneiss were experimentally impacted (Figures 1a and 1b). The metamorphic foliation was vertical, that is, oriented perpendicular to the target surface in the first (experiment A38), and horizontal, that is, parallel to the target surface in the second (experiment A37). Cratering efficiency (the ratio of excavated mass to the projectile mass) is compared between both experiments. The variation in strain below the two impact craters with distance from the point source and with a change in angle between shock front and foliation is determined. The results also show the effects of interaction between the shock wave and the free target surface. The relationships between strain, kink geometry, shock wave propagation direction, and orientation of the foliation are determined.

2. Material and Methods

2.1. Target Material

We picked Maggia gneiss (of Valle Maggia, Switzerland) to represent layered strata. It has 1–3 mm large grains, out of which ~50% are plagioclase, ~40% biotite, and ~8% quartz. Pyroxene, muscovite, and epidote are accessory phases. Plagioclase and biotite grains are millimeter sized and subhedral in form. Both albite and pericline twins are common in plagioclase. Secondary minerals indicating weathering or hydrothermal alteration are absent. In general, the grain boundaries are sharp and well defined, which further precludes alteration. The plagioclase-plagioclase grain boundaries are always irregular. While some plagioclase-biotite grain boundaries are irregular, others are straight. The Maggia gneiss has a density of 2.78 g/cm^3 (Agarwal et al., 2019). It was selected for the experiments because of its no porosity and well-developed planar, 1–2 mm thick, and metamorphic foliation (Figures 1b, 1c, S3, and S4). The foliation is very homogeneous and planar throughout the target blocks and provides a heterogeneity and material contrast in the layering. The layering is smaller than the diameter of the projectile and the resulting crater depths and diameters (Figures 1 and 2a). The metamorphic lineation is not very prominent. Quasi-static uniaxial compressive experiments with the direction of compression parallel with the
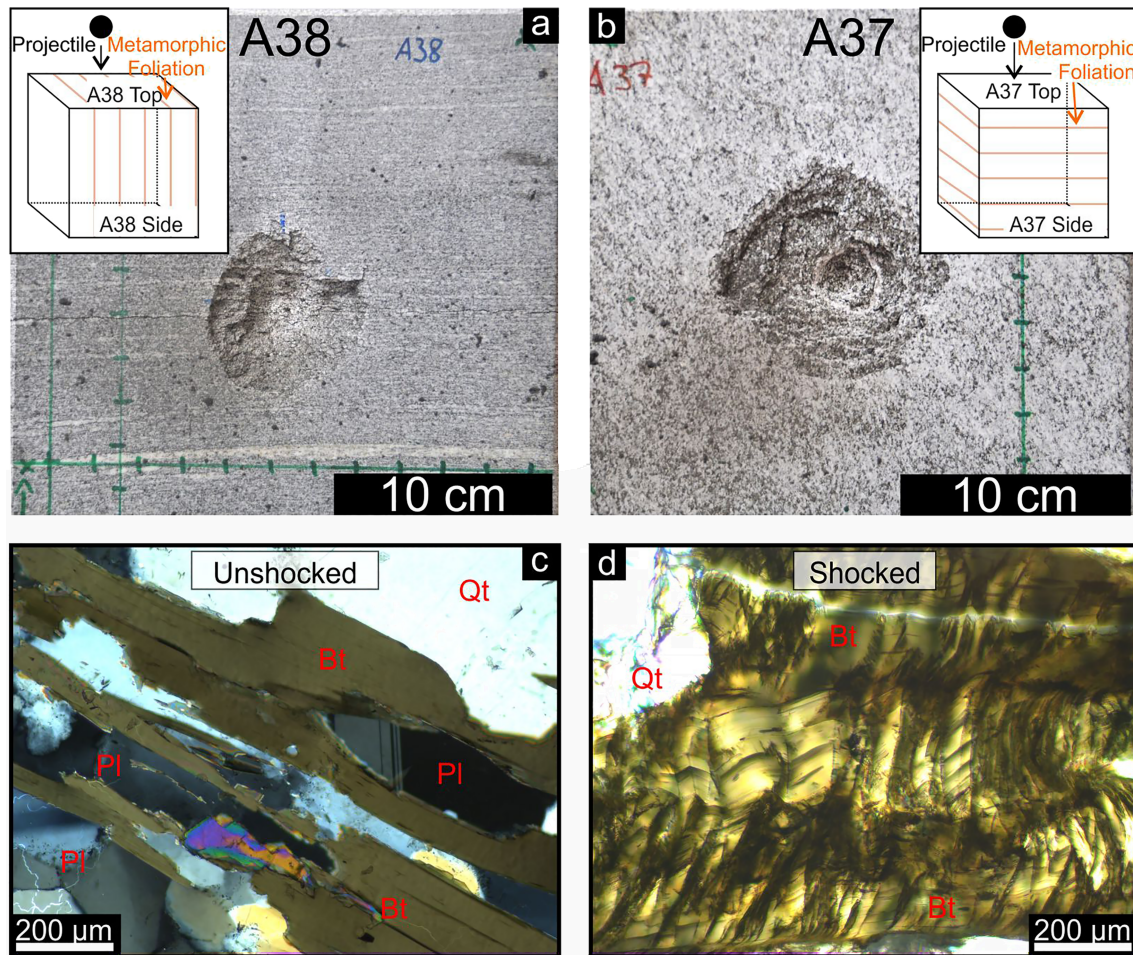
Figure 1. (a and b) Photographs of the craters formed after the impact experiments, with different crater size, crater depth, and crater wall slope of the crater walls. Foliation is perpendicular to the target surface in A38 and parallel in A37. (c and d) Cross-polarized photomicrographs showing bands of undeformed biotite (Bt) bordered on either side by lighter bands of plagioclase (Pl) and quartz (Qt), and the intense kinking due to impact cratering.

foliation and average strain rate (average for one experiment) of $= 7.58 \times 10^{-6} \pm 1.58 \times 10^{-6}$/s were done on five cylindrical samples. The aspect ratio of the cylinders was ~2:1 (see supporting information Table S1 for details). The Quasi-static uniaxial compressive strength, when the direction of compressions is parallel with the foliation, is 153.8 ± 21.0 MPa (1 sigma error) with a Young's modulus of 44.4 ± 1.53 GPa and a Poisson's ratio of 0.209 ± 0.027. Brazilian disk tensile experiments, carried out parallel and perpendicular to the foliation, show little difference at 7.0 ± 2.2 and 7.1 ± 1.2 MPa, respectively (see supporting information Table S2 for details).

2.2. Experimental Setup

Two cubes of Maggia gneiss with 25 cm edge length were used for impact cratering experiments. The foliation was vertical, that is, perpendicular to the target surface, in experiment A38, and horizontal, that is, parallel to the target surface, in experiment A37 (Figures 1a and 1b). Impact experiments were done within the framework of MEMIN (Multidisciplinary Experimental and Modeling Impact Research Network) with a two-stage space light-gas gun (SLGG) at the Fraunhofer Ernst Mach Institute for High-Speed Dynamics in Freiburg, Germany. SLGG accelerated 5 mm, 0.177 g aluminum 55XG28J3 spherical projectiles. This is a specific Al/Cu/Mg/Si alloy. The projectiles were accelerated to 7.236 and 6.925 km s^{-1}, and the target chamber pressure was 1.7 and 1.9 mbar during the experiment on A38 and A37, respectively. Such experiments produce craters with similar dimensions, when the target and projectile properties are constant. Comparison of similar cratering experiments reveals that in cases when all the parameters related to the
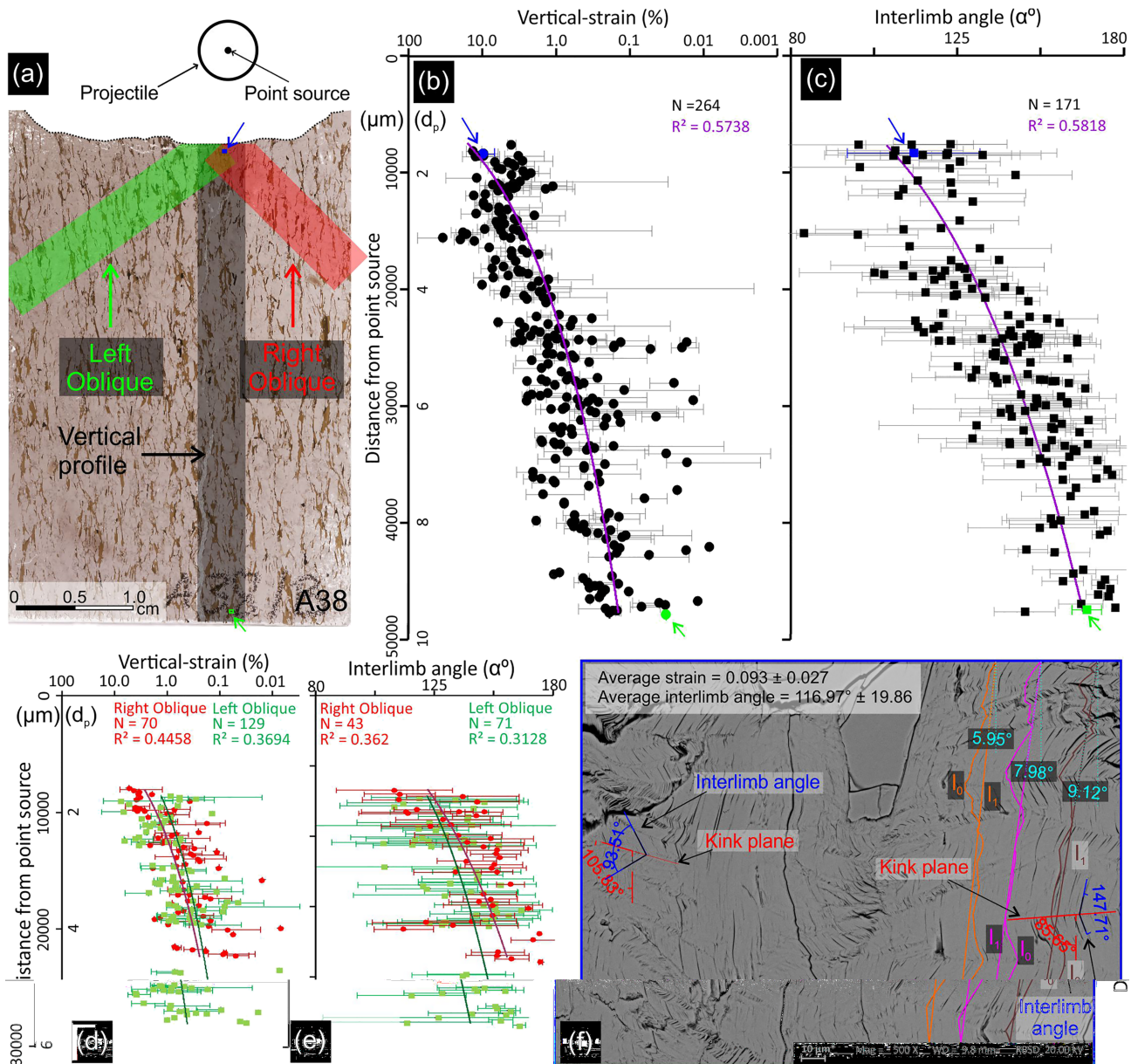
Figure 2. (a) Scan of the thin section made below the impact crater in A38 (vertical foliation) shows the calculated position of the projectile at maximum penetration, the point source, and the Vertical, Left Oblique, and Right Profiles. (b–e) Graphs show the decrease in vertical-strain and increase in interlimb angle with distance from the point source in the three profiles of A38. "*N*" is the number of data points, each representing an average of all measurements in one BSE image. (f) The BSE image, as an example, shows the biotite kinking just below the crater floor. Its position is marked in (a)–(c) in blue. The image also presents the scheme of strain analysis, with three l_0-l_1 pairs and two calculations of interlimb angle (in blue) and of kink plane (in red).

projectile and the target are constant, the resultant craters have comparable dimensions. However, the projectile velocities are rarely same in two experiments; there is always a slight variation, leading to slight variation in crater dimension as well (see supporting information Table S3 to compare crater volume). Experimental cratering procedures are detailed in Kenkmann et al. (2018) and the references therein. Note that a large number of experiments with similar or higher impact velocities, and thus higher impact energies, reveal that the reflections of the shock wave at the block sides can lead to the formation of large tensile fractures parallel to the side walls (Kenkmann et al., 2018). However, this back reflection has no influence on the final macroscopic crater morphology. Within the crater subsurface, a general damage of the target along grain boundaries occurred, which can be slightly amplified by the reflections of the shock wave (Raith et al., 2018).

The equivalent depth of burst (Melosh, 1989) is

$$d_b = d_p \sqrt{\frac{\rho_p}{\rho_t}}$$

where d_p is the projectile diameter (5 mm), ρ_p is the projectile density (2.7 g/cm^3), and ρ_t is the target density (2.8 g/cm^3). It is identical for both experiments at 5 mm.

2.3. Determination of Crater Dimension

Crater topography was determined by a 3-D laser scanner with 100 μm spatial resolution (3-D Digital Corporation, United States). The craters were scanned from 4 to 6 different angles along 18 transects. A digital elevation model was prepared, which provides the dimensions and volume of the cavity. The models estimate the volume with 0.75 to 3.7 vol % error. For details on this method see Dufresne et al. (2013).

2.4. Determination of Net Compressive Strain

Blocks from experiment A38 (vertical metamorphic foliation, that is, oriented perpendicular to the target surface) and experiment A37 (horizontal metamorphic foliation, that is, oriented perpendicular to the target surface) were sawn in half at the crater center, with the sawn surface in both cases perpendicular to the foliation. Thin sections were prepared perpendicular to the metamorphic foliation and the target surface, such that they cover the entire crater subsurface to a distance of 4 cm.

For the quantitative analysis of strain, backscattered electron (BSE) images were captured with a field emission scanning electron microscope, LEO 1525. Lower magnification (29X) overview BSE images were first taken to carefully define the most suitable profiles and mark the appropriate biotite grains for further detailed strain analysis. Three profiles were defined in experiment A38 (vertical foliation) below the impact crater (Figures 2 and S2). They are named Left Oblique, Vertical, and Right Oblique. Since the biotite basal planes are vertical in A38, the measured strain is referred to as vertical strain. Three similar profiles were defined in experiment A37 (horizontal foliation; Figures 4 and S4). They are called Vertical, Left Oblique, and Right Oblique Profiles. The strain was estimated in three more profiles in A37 called Horizontal-1, Horizontal-2, and Interference Profile (Figures 4 and S3). Since the biotite basal planes are horizontal in A37, the measured strain is referred to as horizontal strain. The initial length (l_0), measured by tracing the kink bands, and the final length (l_1), measured as the shortest distance (Figure 2f), give the compressive strain (e) according to the equation

$$e = \frac{(l_0 - l_1)}{l_0}$$

In total 1,337 pairs of l_0 and l_1 are measured. The angle of the l_1 line is measured with respect to the vertical in A38 and the horizontal in A37 (e.g., Figure 2f). The l_1 lines deviating >15° from the vertical in A38 and from horizontal in A37 were discarded. Small zones of intense kinking, representing pockets of high strain, may adversely affect the interpretations. To avoid this, the strain is measured for a constant area, that is, the l_0 and l_1 are always measured from end to end of the BSE image (e.g., Figure 2f). As the magnification of BSE images is 500X, the area covered is constant throughout the analysis. Moreover, 2 to 5 l_0 and l_1 pairs are measured in each BSE image, and their average and the standard deviation are presented.

A power law fit was calculated for the variation in strain and the interlimb angle with distance from the point source. R^2 presents the variance of the data from this fit. The power law exponent defines the decay function of the strain and the growth function of the interlimb angle with distance from the point source.

It is important to note that a spherically outward radiating shock wave front is assumed. Thus, the minor (shortening) axis of the strain ellipse is assumed to be radial to the point source. However, the strain measured from the kinking is along the biotite foliation (vertical strain and horizontal strain) and therefore represents a component of net strain (e). The angle of the biotite foliation to the point source is used to solve the equation of strain ellipse, separately in A37 and A38. Assuming no volume change, the principal strain axes ($e_1 \geq e_2$) are calculated. Here e_1 is the principal axis of elongation and e_2 is the principal axis of shortening. Further details of stain analysis are provided in the supporting information Text S1.
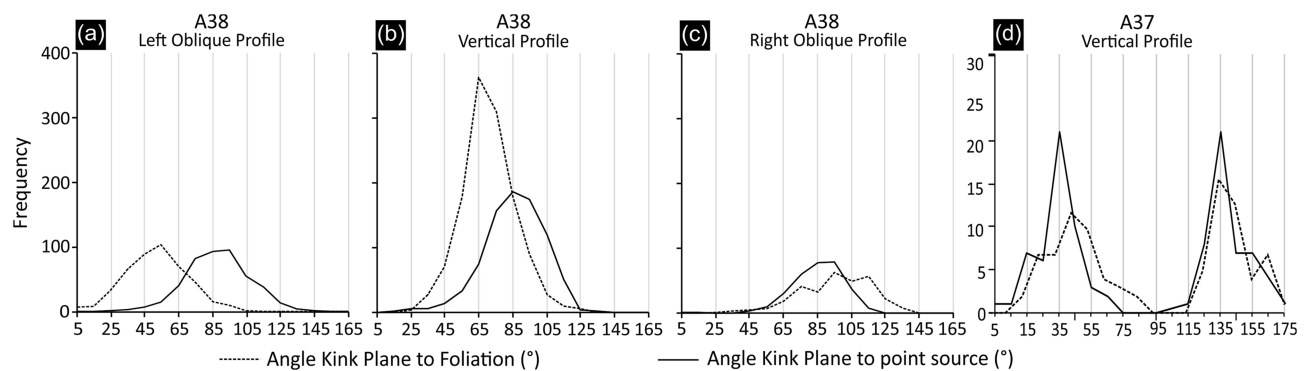
Figure 3. (a–d) Histograms presenting the frequency distribution of the angle of the kink plane to the foliation (dashed) and to the point source (solid).

The e_2 is used to construct strain anisotropy maps. The maps are prepared by using the Inverse Distance Weighting (IDW) interpolation of the ArcGIS software package. Contouring was accomplished by employing 10 quantile classes. A high-resolution map with the scanned target in the background, showing the position of each high magnification BSE image, is provided as supporting information (A38—Figure S3 and A37—Figure S4).

2.5. Analysis of Kink Geometry

Change in the geometry of the kink bands with distance from the point source was investigated by measuring the interlimb angle (Ramsay, 1967; Srivastava et al., 1998, 1999) and the orientation of the kink plane with respect to the point source, which was assumed to be the direction of maximum principal stress (Figures 2 and 3f). The thin sections were prepared perpendicular to the foliation and to the basal plane of the biotite. The kink planes are perpendicular to the plane of view. To average over local intensely kinked zones, 3–10 interlimb angles and kink plane orientation are measured in one BSE image, and their average and standard deviation are presented. The frequency distribution of the angle between the kink plane and the foliation and of the angle between the kink plane and point source is investigated by plotting frequency versus angle histograms. This reveals the control of the biotite orientation and of the shock waves radiating out hemispherically from the point source on the geometry of the kink bands (for details see supporting information Text S2). In this study, results from the measurement of 1,593 interlimb angles and 1,619 kink planes are reported.

3. Results

3.1. Experimental Crater Dimensions and Cratering Efficiency

The crater in experiment A38 with vertical foliation is smaller and shallower than the crater in experiment A37, with horizontal foliation (Figures 1a and 1b). The crater in A38 has steeper walls compared to A37. The latter has a stepped cross-sectional profile. The depth to diameter (d/D) ratio is 0.20 ± 0.03 and 0.21 ± 0.05 for A38 and A37, respectively. The cratering efficiency in A38 (295.7) is lower than in A37 (414.6).

Using the planar impact approximation (Melosh, 1989), a peak shock pressure of at least 88 GPa is calculated at the point of impact. However, most of the material that experienced high shock pressures is excavated or spalled. At the crater floor, depth of approximately 1.7 cm, the peak shock pressure has decayed to <2 GPa (see supporting information Text S2 for details).

3.2. Kink Plane Orientation

Just below the crater floor in A38 (vertical foliation) kink planes within a particular grain differ in orientation (Figures 2a and 2f). Here parallelism among kink bands is restricted to a small domain within a grain. The parallelism improves farther away from the immediate crater floor. Near the crater floor, most kinks do not retain a constant width because they intersect with other neighboring kinks. They thicken, thin or die out into wedge-shaped terminations. As the density of kinks decreases with distance from the crater, many kinks preserve a constant width. Symmetric and asymmetric kinks are common (Figure 2f).
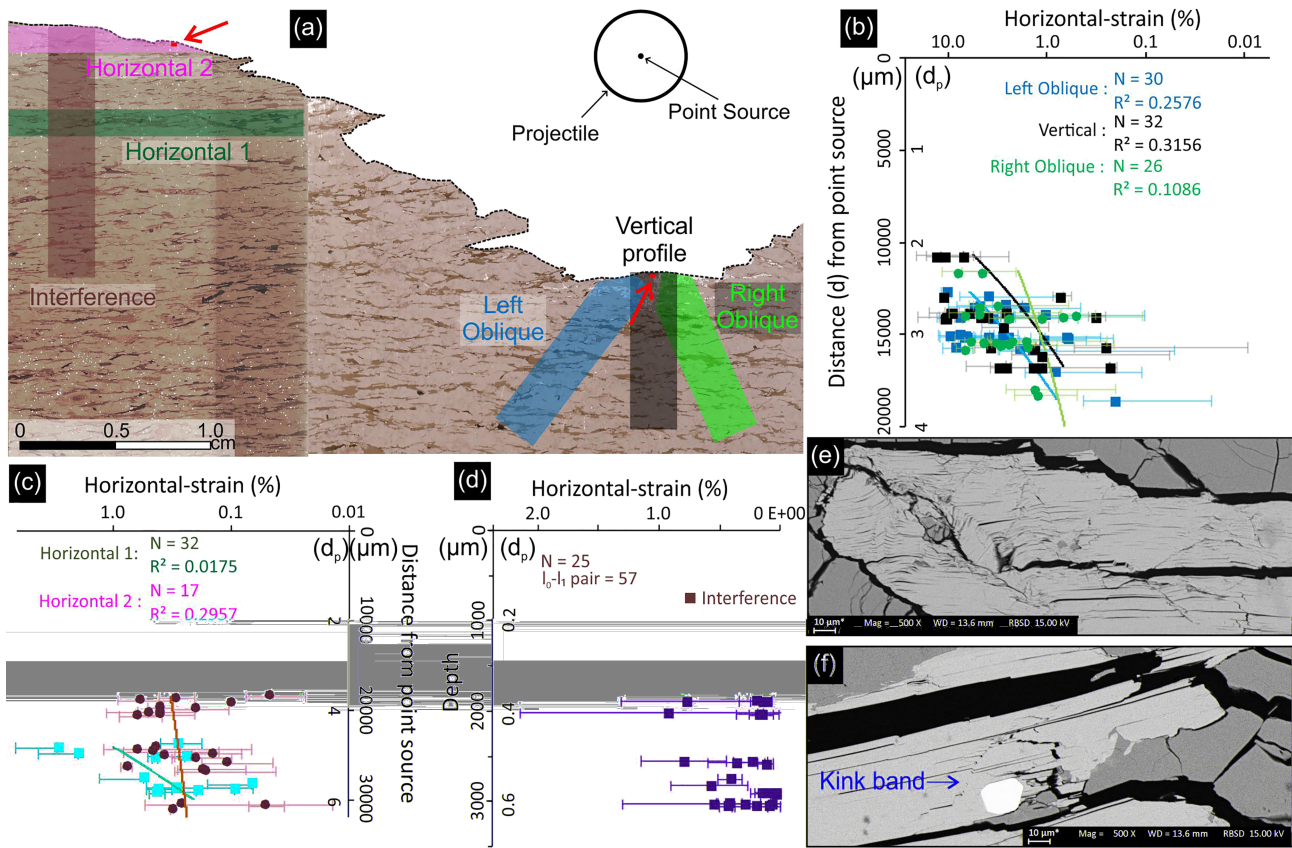
Figure 4. (a) Scan of two thin sections made around the impact crater in A37 (horizontal foliation) shows the calculated position of the projectile at maximum penetration, the point source, and six strain profiles, and the position of the BSE images (e) and (f). (b–d) Graphs show the variation in horizontal-strain with distance from the point source in six profiles of A37. N is the number of data points in the graph, each representing an average of all strain measurements in one BSE image. (e) BSE image of deformed biotite at the crater floor in the Vertical Profile, presenting numerous conjugate kink bands and tensile fractures. (f) BSE image of biotite at the crater wall in Horizontal-2 Profile, presenting a single kink band and tensile fractures.

In the Vertical Profile of A38, the angle between kink planes and the point source varies between 15.8° and 129.8° (Figure 3). In the Left and Right Oblique Profile, it varies between 20.2–143.6° and 10–119.1°, respectively. In all three profiles, the maxima are at ~90°, revealing the perpendicular relationship between the kink plane and the expected shock front propagation direction, assumed to be radiating outward from the point source. The angle between the kink plane and the foliation varies between 20.6–124.7°, 6.2–103.9°, and 21.7–136.9° for the Vertical, Left Oblique, and Right Oblique Profile, respectively, while the means are at 69° ± 15°, 52° ± 17°, and 97° ± 21° (Figure 3). Thus, the angle between foliation and the kink plane varies with the orientation of the shock front.

In A37, (horizontal foliation) beneath the central crater floor, most kinks are asymmetric (Figure 4e). The limbs in kink bands that form conjugate sets dip in opposite directions. With increasing depth below the crater floor, the conjugate sets are less abundant, owing to the general decrease in the density of kinks. At the sides of the crater wall, below the target surface, the kinks are asymmetric, with the shorter limbs mostly dipping opposite to the foliation (profiles Horizontal-1 and Horizontal-2, Figure 4f).

In the Vertical Profile of A37, the orientation of the kink planes with respect to the foliation presents maxima at 40–50° and 130–140° (Figure 3d), while the angle between the kink planes and the point source has two maxima, at 30–40° and 130–140° (Figure 3d). Statistical analysis was not possible for other profiles of A37 because there were only a few kink bands per grain.

3.3. Kink Geometry and Strain

In both A38 and A37, the kink bands are more numerous near the crater floor and their number decreases with distance from the point source. Furthermore, the kinks are tighter near the crater floor and become

Table 1

"l_0-l_1 Pair" and "Kinks Measured" Present the Total Number of Measurements of Strain and Interlimb Angle in Each Profile, Respectively

Profile	l_0-l_1 pairs measured	Kinks measured	Decay function of average strain	Growth function of interlimb angle
A38 Vertical	643	820	−2.6	0.2
A38 Left Oblique	208	472	−1.9	0.2
A38 Right Oblique	137	301	−2.4	0.2
A37 Vertical	62	—	−4.7	—
A37 Left Oblique	58	—	−5.4	—
A37 Right Oblique	79	—	−2	—
A37 Horizontal-1	66	—	−7.3	—
A37 Horizontal-2	27	—	−0.6	—
A37 Interference	57	—	—	—

Note. The decay function of average strain and the growth function of interlimb angle in each profile are also summarized.

gentler with distance (Figures 2c and 2e). In A37 (horizontal foliation), parts of the Horizontal-1 and Horizontal-2 Profiles and Interference Profile reveal geometrically similar kinks. However, the Oblique, Vertical, and Right Oblique Profiles show conjugate sets of kink bands near the crater (Figures 3d and 4e).

In the Vertical Profile of A38 (vertical foliation) the shock wave traverses along the foliation (Figure 2). In this profile, just below the crater floor (~1.6 d_p from the point source; 1 d_p = 5 mm), high vertical strain >13% corresponds with intense kinking such that entire biotite grains are covered with tight kinks (interlimb angles ~85°). With increasing depth, decrease in strain is accompanied by a reduction in density of symmetric and asymmetric kinks. Further below at ~9.3 d_p below the point source, very low vertical strain (0.01%) is accompanied with few gentle folds in biotite (interlimb angle ~177°). The strain in the Oblique Profiles of A38, near the crater surface, is lower than in the Vertical Profile and decrease rapidly with depth (Table 1 and Figure 2). Notably, conjugate kink band sets are not observed at any depth in A38 below the crater.

In the Vertical Profile of A37 (horizontal foliation) the shock wave passes perpendicular to the foliation (Figure 4). Here horizontal strain values of ~10% are accompanied by numerous asymmetric kink bands, some of which form conjugate sets (Figure 4). In this profile, horizontal strain decreases much more rapidly than A38 (Table 1). Below the point source, at depth of ~3.4 d_p, low horizontal strain (~0.3%) is accompanied by gentle folds and few asymmetric kink bands, most of which are concentrated near grain boundaries and other heterogeneities.

The Horizontal-1 and Horizontal-2 Profiles of A37 (horizontal foliation) are located adjacent to the crater wall, in the spallation zone parallel with the shocked surface (Figure 4). In these profiles, the shock wave passes along the foliation, which is similar to the situation in the Vertical Profile of A38. They reveal low horizontal strain, and the kink bands are similar to those in the weakly strained parts of the Vertical Profile of A38.

These results show a clear correlation between strain and interlimb angles. Higher amounts of shortening are reached through tighter folding in the kinks and narrower interlimb angles. The strain decreases and the interlimb angle increases with distance from the point source in all profiles of A37 and A38 (Figures 2 and 4 and Table 1). Individual strain and the interlimb angle data present large scatter.

The distribution of strain within a single grain is investigated in 20 biotites (Figure 5). About 70% of biotite grains are strained more at the top and bottom than in the middle. Out of these, six grains are strained more in the bottom part than in the top part. In just two grains, the strain is highest in the middle part and the lowest at the bottom (grain 4 and 14).

3.4. Anisotropy of Strain

The measured vertical strain in A38 and horizontal strain in A37 represent strain in a single direction, corresponding to the orientation of the biotite grains. Using the measured strain and the angular relationship
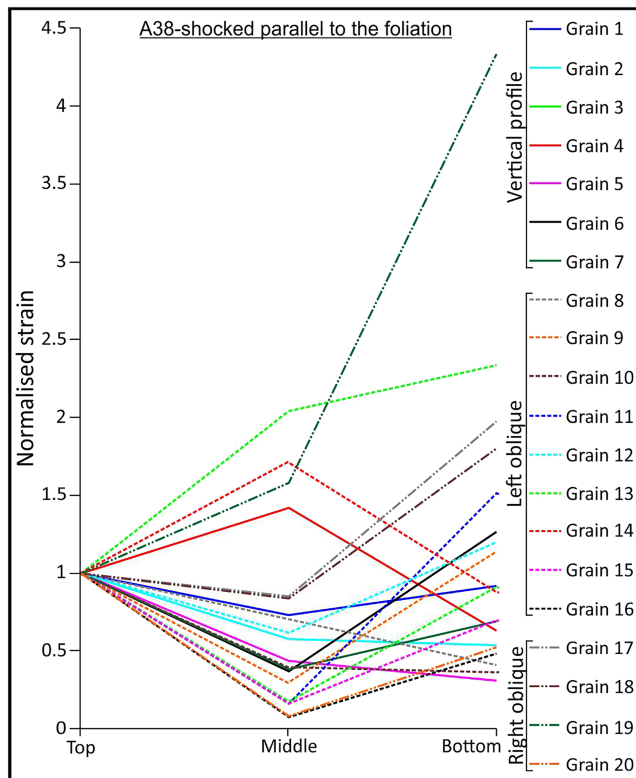
Figure 5. The graph presents the strain within the middle and bottom part of individual biotite grains, normalized to the top part. Approximately 70% of the 20 grains measured are strained more at the top and bottom as compared to the middle.

between biotite grains and the point source, the principal axes of the strain ellipsoid e_1 and e_2 are defined in both magnitude and orientation (see supporting information Text S3 for details).

In A38, the shortening direction e_2 is radial while e_1 is concentric below the crater (Figure 6). In general, strain decreases with distance from the point source. A zone of intense deformation stretches vertically below the impact crater along the petrographic foliation (red in Figure 6). The shortening e_2 in the Vertical Profile is 38% and 95% more than in the Left and Right Oblique Profiles, respectively. The maximum shortening e_2 decreases sharply with distance from the point source, while in the Vertical Profile it decreases gradually.

Experiment A37 (horizontal foliation) shows a fundamentally different pattern of strain with respect to A38. First, the principal axes are flipped so that the elongation axes e_1 is oriented radially, whereas the shortening direction e_2 is trending concentric with respect to the point source (Figure 6). This is because in A37 horizontal layering of biotite grains allows compression in the horizontal direction, and low kinking corresponds with weak dampening of the shock wave, thus allowing strong reflections. The reflections cause tensile fracturing, which leads to an extension in a vertical direction. Second, the magnitude of compressive strain is an order of magnitude lower than in experiments A38 (Figure 6).

The six profiles in experiment A37 allow comparison of strain below and adjacent to the crater. The strain is higher below the crater than at the side (Figure 6). In general, the strain decreases with depth below the crater floor. In the strain anisotropy map below the crater floor, the strain is highest in the left part as compared to the central and right part. In the spallation zone, left of the crater in A37, a small region of high strain is attributed to a local shear zone (Figure 6). Except for this zone, strain in both the Horizontal-1 and Horizontal-2 Profiles and the Interference Profile is low.

4. Discussion

The effects of mechanical heterogeneities in the target rocks on the morphology of the craters and the subsurface deformation are among the least understood aspects of impact cratering. The only established techniques to investigate subsurface deformation over a large range of depths are either drilling into the crater or numerical modeling. While the former is very expensive, and therefore not very common, the later has only recently started to implement mechanical anisotropy of the target rocks (e.g., Hopkins et al., 2019). However, mechanically heterogeneous targets are very common throughout the solar system.

Generally craters with polygonal outline are attributed to anisotropic targets, for example, Meteor crater (Poelchau et al., 2009; see also Eppler et al., 1983; Öhman, et al., 2006). There are numerous (dozens) of craters that are formed in targets with bedding parallel sedimentary layers with high competence contrasts. Two examples are Jebel Waqf as Suwwan, Jordan (Kenkmann et al., 2015), where buckling instabilities in the form of kink and chevron folds developed (chert interlayered with marly limestone), and Upheaval Dome, where faults develop parallel to the layers and lead to a disintegration into bedding parallel slices (Kenkmann et al., 2005). Although a sedimentary target with vertical beds prior to impact is uncommon, there are 55 craters with anisotropic gneiss and 23 craters with schist as one of the target lithologies (Kenkmann, 2019). In many of these the foliation is oriented at high angle to the surface, for example, the mylonitic foliation in Suvasvesi North, Finland (Kenkmann, 2019).

The present study, therefore, reports the subsurface deformation and the morphology of two experimental craters in Maggia gneiss with layers presenting a mechanical contrast. Three-dimensional laser scans
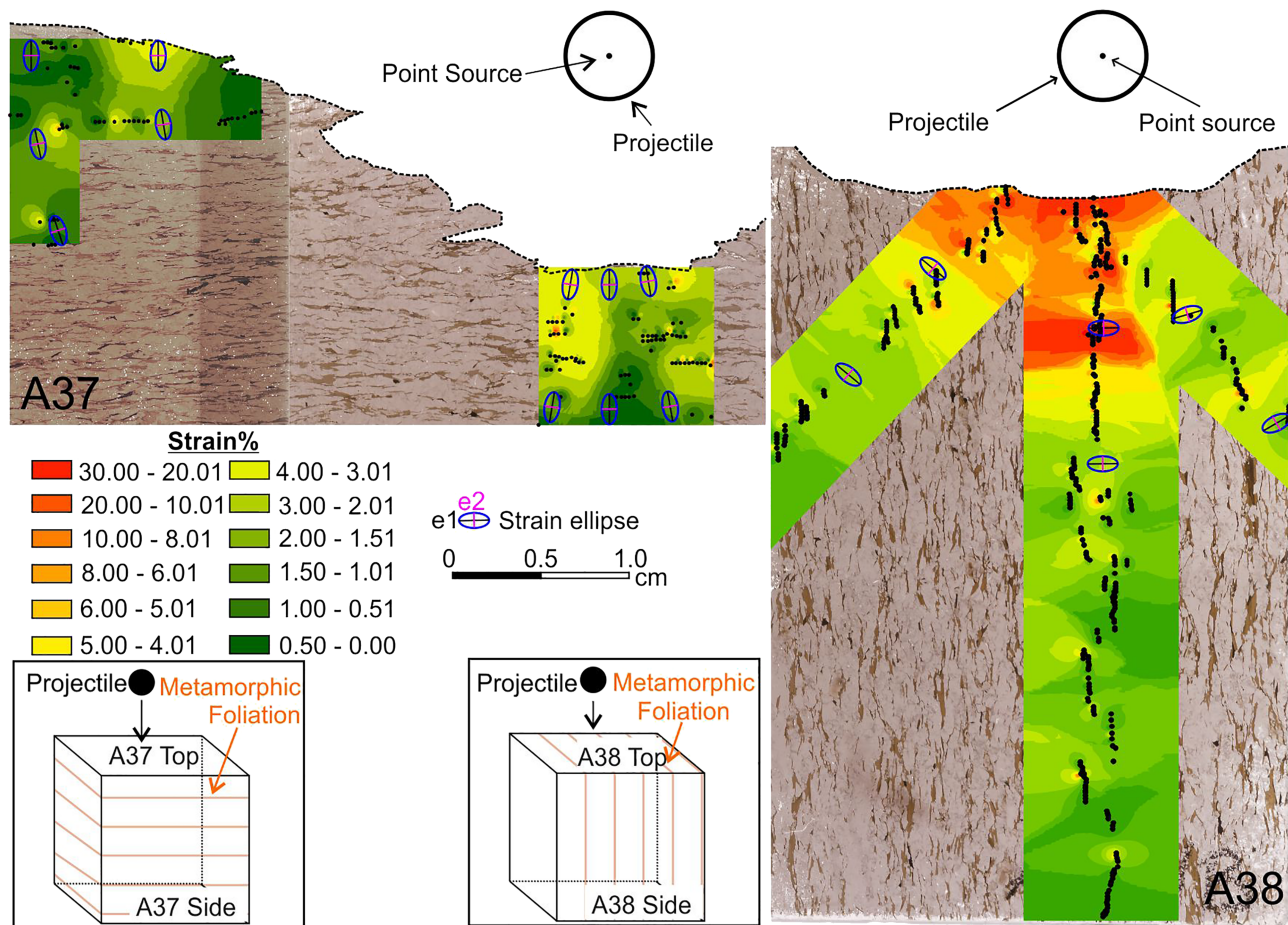
Figure 6. Strain anisotropy map of A37 (left) and A38 (right), with horizontal and vertical foliation, respectively. The percentages refer to strain in the direction of the principal axis of the strain ellipse. The data points are shown with the black dots. The projectile and the point source are shown at the estimated burial depth.

quantify the morphology of the craters, and comprehensive analysis of kink band geometry (interlimb angle and kink plane orientation) and detailed strain analysis reveals the subsurface deformation.

4.1. Kink Band Geometry

Our present results reveal that the angle between the foliation and the kink plane depends upon the location with respect to the point source. The situation is explained with a sketch showing the orientation of the majority of kink planes with respect to the point source (Figure 7). If the shock front propagates perpendicular to the biotite basal plane (as in the Vertical Profile of A38), symmetric kink bands develop and the kink plane, line bisector of the interlimb angle, mimics the orientation of shock front. If the shock front propagates obliquely at high angles (>70°) to the biotite basal planes as it is the case for the oblique profiles in A38, asymmetric kink bands form with a short limb and a long limb. The kink plane is no longer the bisecting line of the interlimb angle. The kink plane still corresponds to the shock front that spreads out hemispherically from the point source.

Previously reported shock experiments (10–40 kbar) on single crystal lepidomelane have revealed a similar relationship between the kink planes and the maximum principal stress (Hörz & Ahrens, 1969). However, these findings are in contrast to the numerous reports on rocks deformed under experimental or natural static conditions. Under static conditions, with <50% strain, basal slip and ripplocation result in conjugate kink bands, with kink planes at 55–65° to the maximum compression direction (e.g., Aslin et al., 2019; Borg & Handin, 1966; Etheridge et al., 1973; Gay & Weiss, 1974; Paterson & Weiss, 1966). Notably, in the present study, no conjugate sets are observed with shock front perpendicular or at high angles to the foliation
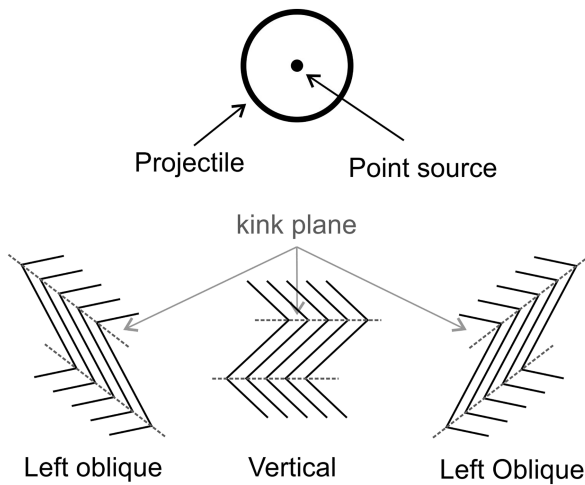
Figure 7. The general orientation of kink plane with respect to the point source.

(Vertical and Oblique Profile in A38). We therefore suggest that the genesis of kink bands under dynamic stresses is different from that under static conditions.

Comparison of measured strain (vertical in A38, and horizontal in A37) with the interlimb angles reveals a clear relationship between the two (Figures 2 and 4). Higher strain and smaller interlimb angles are recorded near the point source. The strain decreases and the interlimb angle increases with distance from the point source. It is therefore summarized that strain is accommodated with kinking of biotite, and higher strain is achieved by tighter kinking.

4.2. Distribution of Strain

A general trend of decrease in strain, with distance from the point source, is conspicuous below the crater. However, the data show significant variability. This variation is owed to three factors. First, the nonelastic deformation of biotite is irregular. Experiments of layer-parallel static compression in biotite show that peak stress corresponds to ~ 2% strain. Thereafter, the curve behaves irregularly, with episodes of strain weakening and strain hardening (Gottschalk et al., 1990; Paterson & Weiss, 1966). The second factor is the termination of the irregular biotite grain boundaries against various grains. The shock wave reflects, refracts, and concentrates (due to impedance matching) at the grain boundaries, thus straining a part of the grain. Third, the local shear zones, which occasionally traverse across biotite, caus localized shearing and kinking in a small part of the grain. Winkler et al. (2018) have reported similar local shear zones beneath experimental impact craters in marble and quartzite. To avoid misinterpretation of strain, such effects have been minimized by measuring strain over a constant area and averaging it by taking several readings. However, they still contribute to the nonsystematic variation in strain with distance from the point source.

The distribution of strain was analyzed within twenty biotite grains in the Vertical, Left, and Right Oblique Profiles of A38 (vertical foliation). The results show that strain is unevenly distributed and is concentrated near the grain interface in agreement with other studies (Heider & Kenkmann, 2003). ~70% of biotite reported here are more strained at the top and bottom compared to the middle. Higher strain at the top of the grain is owed to the stronger shock wave at the top, which loses part of its energy as it travels down the grain. Higher strain at the lower part of the grain may be explained by the superimposing of the deformation by the incident shock wave and its reflected part.

4.2.1. Control of the Foliation on the Compressive Strain

Comparison of strain anisotropy maps of A38 (vertical foliation) and A37 (horizontal foliation) reveals two important pieces of evidence that clearly demonstrate the control of the foliation on strain (Figure 6). First, the strain below the crater floor in A38 is an order of magnitude higher than in A37. Second, near the crater floor in A38, the highest strain is recorded vertically below the point source, and strain is lower in the grains near the crater floor in the Left and Right Oblique Profiles. On the other hand, in A37 the Vertical Profile has lower strain than the Left Oblique Profile even though the grains in the former are nearer to the point source (Figure 6). These two stark contrasts are owed to the ability of biotite to deform easily along its basal plane (Borg & Handin, 1966; Kronenberg et al., 1990; Shea & Kronenberg, 1993). In agreement, Winkler et al. (2018) proposed that the shape and crystallographic preferred orientations of the mineral constituents may lead to strength anisotropies and complicate the mechanical response to dynamic loading.

Agarwal et al. (2019) investigated the effects of the impact cratering on the magnetic fabrics, by analyzing the same blocks from experiments A37 and A38 as used in the present study. They show that in A38, there is a narrow zone beneath the crater with intense reorientation of magnetic fabrics. Reorientation on either side of this zone is feeble. This zone corresponds spatially with the Vertical Profile of A38. In agreement to the reorientation of the magnetic fabrics, the Vertical Profile of A38 shows intense straining, which is lower on either side, in the Left and Right Oblique Profiles of A38. Agarwal et al. (2019) show that in A37 (horizontal foliation) the reorientation of the magnetic fabrics is less below the crater, but more at the sides. A similar trend is seen in the present study. A37′s Left Oblique Profile reveals a higher strain than the Vertical Profile.

4.2.2. Compressive Strain Below and Adjacent to the Crater

In the Interference Profile of A37 (horizontal foliation), strain increases slightly with depth, which may be due to the effect of the interaction between the tensile and compressive phases of the shock wave in the interference zone (e.g., Melosh, 1989). Horizontal-1 and Horizontal-2 Profiles located in the spallation zone of A37 show only small region of kinking, associated with a local shear zone. This in principle agrees with numerical models, which show a higher magnitude of shock below the impact crater as compared to the sides. At the sides, interaction with the free surface lowers the magnitude of the shock wave (e.g., Pierazzo & Melosh, 2000). The magnetic fabric analysis has also shown concurring results, with more deformation below the crater than at the target surface (Agarwal et al., 2019). Notably, in the two Horizontal Profiles, tensile fractures are more prominent than kinking, revealing the dominance of tensile strain in this region. It may, therefore, be summarized that the tensile strain dominates adjacent to the crater wall, while compressive strain dominates below the crater. Numerical models tend to support these trends (Collins & Melosh, 2004).

4.3. Upscaling

Maggia gneiss was carefully selected for the experiments due to its 1–2 mm thick layering. Impact of a projectile, 5 mm in diameter, formed craters that are 1.4 and 1.8 cm deep and on average 7.1 and 8.5 cm in diameter in A38 and A37, respectively. Dimensions of these experimental craters scale up geometrically. Multiplying these results by a factor of 10,000 gives a simple crater 0.7–0.85 km in diameter and 140 to 180 m deep, with 10–20 m thick stratigraphic layers. This is comparable to natural craters, such as Meteor Crater, United States. Present experiments are, therefore, well applicable to natural scenarios.

Xia and Ahrens (2001) define the maximum damage depth through shock experiments and conclude that the furthest extending fracture is radial. In agreement, radial microfractures are reported as the furthest extending fracture in natural craters, which lack target layers with mechanical contrast, for example, Lonar Crater, India (Agarwal et al., 2016), and Lockne Crater Sweden (Agarwal et al., 2015). However, in the present case the tensile fracture zones extend to a depth of 1 cm ($2\ d_p$) in A38 and to 0.55 cm ($\sim1\ d_p$) in A37. The trend of the tensile fractures is governed by the orientation of the foliation. Present results, therefore, underline the exclusivity of the conclusion of Xia and Ahrens (2001) and imply that when present, the target layering will influence the orientation of the fractures and the maximum damage depth.

Present results show that the deformation is concentrated in the weaker/softer layers. These layers fracture easily under tensile forces, which affects the crater morphology. The crater formed with horizontal layering (A37) is deeper than that formed with vertical layering (A38). This is owed to lesser spallation in A38, where higher kinking intensity causes increased attenuation, and thus weaker reflections of the shock wave. Higher spallation in A37 is also owed to well-defined mechanical heterogeneity due to horizontal layering. Stronger reflections cause tensile fracturing at the crater basement, thus breaking apart the rocks from the crater floor leading to a deeper crater with a flat floor. While the kinking occurs during the initial compression, the tensile fractures form during the later tensile phase of the shock wave. Generally, the reflections are stronger at the boundary between grains with higher mechanical contrast, biotite, and plagioclase in this case. The reflections are stronger near the point of impact and decrease with depth in proportion with the decreasing intensity of the shock wave.

5. Conclusions

This study investigates the deformation in the subsurface of experimentally produced impact craters formed in a mechanically anisotropic layered target. Two endmembers are considered. In one experiment (A37) the layering is parallel (horizontal) to the target surface and in the other (A38) the layering is perpendicular (vertical) to the target surface. The strain is quantified using kink bands in biotite as strain markers. The geometry of kink bands was analyzed by quantifying the interlimb angle and the orientation of the kink plane.

If the shock front is perpendicular or at high angles (>70°) to the foliation, symmetric kink bands develop and the kink plane is in the orientation of shock front. A similar relationship has been shown by Hörz and Ahrens (1969) and Hörz (1970). The kink planes may, therefore, be used as an indicator of shock propagation direction.

If the shock front is parallel to the foliation, the kink bands are conjugate. This is contradictory to static experiments, where layer perpendicular static compression causes no kinking (e.g., Davis et al., 2012;

Etheridge et al., 1973; Paterson & Weiss, 1966; Ramsay & Huber, 1987). In the present case, kinking with shock front parallel to the foliation is attributed to higher strain rates and confining pressure experienced by the rocks during the passage of the shock waves, as compared to the static loading on single crystals.

Notably, the deformation is higher below the crater floor, than adjacent to the crater wall. Furthermore, there is a stark difference in intensity and distribution of deformation below the crater depending upon the orientation of the layering. This anisotropy of deformation/strain underlines the critical effect of the orientation of mechanical heterogeneities such as stratigraphic layering and foliation. Considering the fact that numerical models reveal only slight variations in strain between impact craters in quartzite and marble (Winkler et al., 2018). It is safe to conclude that the subsurface deformation may be controlled more by the orientation of the layering, which provides mechanical heterogeneity, and relatively less by variation in lithology if no significant mechanical contrast exists.

References

Agarwal, A., Kontny, A., & Greiling, R. O. (2015). Relationships among magnetic fabrics, microfractures and shock pressures at an impact crater: A case study from Lockne crater, Sweden. *Journal of Applied Geophysics*, *114*, 232–243. https://doi.org/10.1016/j.jappgeo.2015.01.010

Agarwal, A., Kontny, A., Kenkmann, T., & Poelchau, M. H. (2019). Variation in paramagnetic fabrics due to experimental impact cratering. *Journal of Geophysical Research: Solid Earth*. https://doi.org/10.1029/2018JB017128

Agarwal, A., Kontny, A., Srivastava, D. C., & Greiling, R. O. (2016). Shock pressure estimates in target basalts of a pristine crater: A case study in the Lonar crater, India. *Geological Society of America Bulletin*, *128*(1/2), 19–28. https://doi.org/10.1130/B31172.1

Agarwal, A., Reznik, B., Alva-Valdivia, L. M., & Srivastava, D. C. (2016). Alternating augite-plagioclase wedges in basement dolerites of Lockne impact structure, Sweden: A new shock wave-induced deformation feature. *Meteoritics & Planetary Science*, *52*, 458–470. https://doi.org/10.1111/maps.12806

Agarwal, A., Reznik, B., Kontny, A., Heissler, S., & Schilling, F. (2016). Lingunite-a high-pressure plagioclase polymorph at mineral interfaces in doleritic rock of the Lockne impact structure (Sweden). *Scientific Reports*, *6*, 25991. https://doi.org/10.1038/srep25991

Aslin, J., Mariani, E., Dawson, K., & Barsoum, M. W. (2019). Ripplocations provide a new mechanism for the deformation of phyllosilicates in the lithosphere. *Nature Communications*, *10*(1), 686. https://dx.doi.org/10.1038/s41467-019-08587-2

Baud, P., Louis, L., David, C., Rawling, G. C., & Wong, T.-F. (2005). Effects of bedding and foliation on mechanical anisotropy, damage evolution and failure mode. *Geological Society of London, Special Publication*, *245*, 223–249. https://doi.org/10.1144/GSL.SP.2005.245.01.11

Borg, I., & Handin, J. (1966). Experimental deformation of crystalline rocks. *Tectonophysics*, *3*, 249–367. https://doi.org/10.1016/0040-1951(66)90019-9

Chao, E. C. T. (1967). Shock effects in certain rock-forming minerals. *Science*, *156*(3772), 192–202. https://doi.org/10.1126/science.156.3772.192

Cintala, M.J., Wood, C.A., Head, J.W., 1977. The effects of target characteristics on fresh crater morphology—Preliminary results for the Moon and Mercury, in: Lunar and Planetary Science Conference Proceedings. pp. 3409–3425.

Collins, G. S., Kenkmann, T., Osinski, G. R., & Wünnemann, K. (2008). Mid-sized complex crater formation in mixed crystalline-sedimentary targets: Insight from modeling and observation. *Meteoritics and Planetary Science*, *43*, 1955–1977. https://doi.org/10.1111/j.1945-5100.2008.tb00655.x

Collins, G. S., Melosh, H. J., & Ivanov, B. A. (2004). Modeling damage and deformation in impact simulations. *Meteoritics and Planetary Science*, *39*, 217–231. https://doi.org/10.1111/j.1945-5100.2004.tb00337.x

Cummings, D. (1965). Kink-bands: Shock deformation of biotite resulting from a nuclear explosion. *Science*, *148*, 950–952. https://doi.org/10.1126/science.148.3672.950

Cummings, D., 1968. Shock deformation of biotite around a nuclear explosion. Shock Metamorph. Nat. Mater. Balt. Maryland, Mono B. Corp. 211–218.

Davis, G. H., Reynolds, S. J., & Kluth, C. H. (2012). *Structural geology of rocks and regions, in: Structural geology of rocks and regions* (3rd ed., pp. 736–747). Hoboken, NJ: John Wiley & Sons, Inc.

Dressler, B. (1990). Shock metamorphic features and their zoning and orientation in the Precambrian rocks of the Manicouagan Structure, Quebec, Canada. *Tectonophysics*, *171*, 229–245. https://doi.org/10.1016/0040-1951(90)90101-D

Dufresne, A., Poelchau, M. H., Kenkmann, T., Deutsch, A., Hoerth, T., Schäfer, F., & Thoma, K. (2013). Crater morphology in sandstone targets: The MEMIN impact parameter study. *Meteoritics and Planetary Science*, *48*, 50–70. https://doi.org/10.1111/maps.12024

Eppler, D. T., Ehrlich, R., Nummedal, D., & Schultz, P. H. (1983). Sources of shape variation in lunar impact craters: Fourier shape analysis. *Geological Society of America Bulletin*, *94*, 274–291.

Etheridge, M. A., Hobbs, B. E., & Paterson, M. S. (1973). Experiental deformation of single crystals of biotite. *Contributions to Mineralogy and Petrology*, *38*(1), 21–36. https://doi.org/10.1007/BF00371724

Gay, N. C., & Weiss, L. E. (1974). The relationship between principal stress directions and the geometry of kinks in foliated rocks. *Tectonophysics*, *21*, 287–300. https://doi.org/10.1016/0040-1951(74)90056-0

Gibson, R. L., & Reimold, W. U. (2005). Shock pressure distribution in the Vredefort impact structure, South Africa. In Kenkmann, T., Hörz, F., Deutsch, A. (Eds.), Special *Paper 384: Large meteorite impacts III*, *Geological Society of America* (pp. 329–349). Boulder, CO: Geological Society of America. https://doi.org/10.1130/0-8137-2384-1.329

Gohn, G. S., Koeberl, C., Miller, K. G., Reimold, W. U., Browning, J. V., Cockell, C. S., et al. (2008). Deep drilling into the Chesapeake Bay impact structure. *Science*, *320*(5884), 1740–1745. https://doi.org/10.1126/science.1158708

Gottschalk, R. R., Kronenberg, A. K., Russell, J. E., & Handin, J. (1990). Mechanical anisotropy of gneiss: Failure criterion and textural sources of directional behavior. *Journal of Geophysical Research*, *95*, 21613. https://doi.org/10.1029/JB095iB13p21613

Grieve, R.A.F., Robertson, P.B., Dence, M.R., 1981. Constraints on the formation of ring impact structures, based on terrestrial data, in: Multi-ring basins: Formation and evolution. pp. 37–57.

Heider, N., & Kenkmann, T. (2003). Numerical simulation of temperature effects at fissures due to shock loading. *Meteoritics and Planetary Science*, *38*, 1451–1460. https://doi.org/10.1111/j.1945-5100.2003.tb00250.x

Hopkins, R. T., Osinski, G. R., & Collins, G. S. (2019). Formation of complex craters in layered targets with material anisotropy. *Journal of Geophysical Research: Planets*, *124*, 349–373. https://doi.org/10.1029/2018JE005819

Hörz, F. (1970). Static and dynamic origin of kink bands in micas. *Journal of Geophysical Research*, *75*, 965–977. https://doi.org/10.1029/JB075i005p00965

Hörz, F., & Ahrens, T. J. (1969). Deformation of experimentally shocked biotite. *American Journal of Science*, *267*, 1213–1229. https://doi.org/10.2475/ajs.267.10.1213

Joshi, G., Agarwal, A., Agarwal, K. K., Srivastava, S., & Alva-Valdivia, L. M. (2017). Microstructures and strain variation: Evidence of multiple splays in the North Almora Thrust Zone, Kumaun Lesser Himalaya, Uttarakhand, India. *Tectonophysics*, *694*, 239–248. https://doi.org/10.1016/j.tecto.2016.11.008

Kenkmann, T., 2019. Update of the terrestrial impact crater record: Crater discovery statistics, size and age frequency distributions. Large Meteorite Impacts VI 2019 (LPI Contrib. No. 2136).

Kenkmann, T., Deutsch, A., Thoma, K., Ebert, M., Poelchau, M. H., Buhl, E., et al. (2018). Experimental impact cratering: A summary of the major results of the MEMIN research unit. *Meteoritics and Planetary Science*, *53*, 1543–1568. https://doi.org/10.1111/maps.13048

Kenkmann, T., Hornemann, U., & Stöffler, D. (2000). Experimental generation of shock-induced pseudotachylites along lithological interfaces. *Meteoritics and Planetary Science*, *35*, 1275–1290. https://doi.org/10.1111/j.1945-5100.2000.tb01516.x

Kenkmann, T., Jahn, A., Scherler, D., Ivanov, B. A., 2005. Structure and formation of a central uplift: A case study at the Upheaval Dome impact crater, Utah. Large meteorite impacts III, 85-115.

Kenkmann, T., et al. (2015). Jebel Waqf as Suwwan, Jordan: Results of a Field Campaign 2015. In *Bridging the Gap III: Impact Cratering In Nature, Experiments, and Modeling* (Vol. 1861).

Kring, D. A., Hörz, F., Zurcher, L., & Urrutia Fucugauchi, J. (2004). Impact lithologies and their emplacement in the Chicxulub impact crater: Initial results from the Chicxulub Scientific Drilling Project, Yaxcopoil, Mexico. *Meteoritics and Planetary Science*, *39*, 879–897. https://doi.org/10.1111/j.1945-5100.2004.tb00936.x

Kronenberg, A. K., Kirby, S. H., & Pinkston, J. (1990). Basal slip and mechanical anisotropy of biotite. *Journal of Geophysical Research*, *95*, 19257. https://doi.org/10.1029/JB095iB12p19257

Lisle, R. J. (1985). *Geological strain analysis: A manual for the Rf/ø method*. Amsterdam, Netherlands: Elsevier.

Melosh, H. J. (1989). *Impact cratering: A geologic process*, (11th ed.. Research supported by NASA). New York: Oxford University Press. (Oxford Monographs on Geology and Geophysics)

Melosh, H. J., & Ivanov, B. A. (1999). Impact crater collapse. *Annual Review of Earth and Planetary Sciences*, *27*, 385–415.

Ogilvie, P., Gibson, R. L., Reimold, W. U., Deutsch, A., & Hornemann, U. (2011). Experimental investigation of shock metamorphic effects in a metapelitic granulite: The importance of shock impedance contrast between components. *Meteoritics and Planetary Science*, *46*, 1565–1586. https://doi.org/10.1111/j.1945-5100.2011.01250.x

Öhman, T., Aittola, M., Korteniemi, J., et al. (2010). Polygonal impact craters in the solar system: Observations and implications. *Geological Society of America Special Papers*, *465*, 51–65.

Öhman, T., Aittola, M., Kostama, V. P., Hyvärinen, M., & Raitala, J. (2006). Polygonal impact craters in the Argyre region, Mars: Evidence for influence of target structure on the final crater morphology. *Meteoritics & Planetary Science*, *41*(8), 1163–1173.

Ormö, J., & Lindström, M. (2000). When a cosmic impact strikes the sea bed. *Geological Magazine*, *137*, 67–80.

Osinski, G. R., & Pierazzo, E. (2012). *Impact cratering: Processes and products*. Hoboken, NJ: John Wiley & Sons.

Paterson, M. S., & Weiss, L. E. (1966). Experimental deformation and folding in phyllite. *Geological Society of America Bulletin*, *77*, 343–374.

Pierazzo, E., & Melosh, H. J. (2000). Understanding oblique impacts from experiments, observations, and modeling. *Annual Review of Earth and Planetary Sciences*, *28*, 141–167. https://doi.org/10.1146/annurev.earth.28.1.141

Pike, R.J., 1980. Control of crater morphology by gravity and target type-Mars, Earth, Moon, in: Lunar and Planetary Science Conference Proceedings. pp. 2159–2189.

Poelchau, M. H., Kenkmann, T., & Kring, D. A. (2009). Rim uplift and crater shape in Meteor Crater: Effects of target heterogeneities and trajectory obliquity. *Journal of Geophysical Research*, *114*, E01006. https://doi.org/10.1029/2008JE003235

Pohl, J., Stöffler, D., Gall, H., & Ernstson, K. (1977). *Ries impact crater. In: Impact and explosion cratering* (pp. 343–404). New York: Pergamon Press.

Quaide, W. L., & Oberbeck, V. R. (1968). Thickness determinations of the lunar surface layer from lunar impact craters. *Journal of Geophysical Research*, *73*, 5247–5270. https://doi.org/10.1029/JB073i016p05247

Raith, M., Ebert, M., Pinkert, K., & Grosse, C. U. (2018). Nondestructive imaging of hypervelocity impact-induced damage zones beneath laboratory-created craters by means of ultrasound travel-time tomography. *Meteoritics & Planetary Science*, *53*(8), 1756–1772. https://doi.org/10.1111/maps.13113

Ramsay, J. G. (1967). *Folding and fracturing of rocks*. New York City: McGraw-Hill Companies.

Ramsay, J. G., & Huber, M. I. (1983). *The techniques of modern structural geology: Strain analysis* (Vol. 1). London: Strain Anal. Acad. Press.

Ramsay, J. G., & Huber, M. I. (1987). *The techniques of modern structural geology: Folds and Fractures*. Cambridge, MA: Academic Press.

Riller, U. (2005). Structural characteristics of the Sudbury impact structure, Canada: Impact-induced versus orogenic deformation—A review. *Meteoritics and Planetary Science*, *40*, 1723–1740. https://doi.org/10.1111/j.1945-5100.2005.tb00140.x

Schneider, H. (1972). Shock-induced mechanical deformations in biotites from crystalline rocks of the ries crater (Southern Germany). *Contributions to Mineralogy and Petrology*, *37*(1), 75–85. https://doi.org/10.1007/BF00377308

Schreyer, W. (1983). Metamorphism and fluid inclusions in the basement of the Vredefort Dome, South Africa: Guidelines to the origin of the structure. *Journal of Petrology*, *24*, 26–47. https://doi.org/10.1093/petrology/24.1.26

Senft, L. E., & Stewart, S. T. (2007). Modeling impact cratering in layered surfaces. *Journal of Geophysical Research*, *112*, E11002. https://doi.org/10.1029/2007JE002894

Shea, W. T., & Kronenberg, A. K. (1993). Strength and anisotropy of foliated rocks with varied mica contents. *Journal of Structural Geology*, *15*, 1097–1121. https://doi.org/10.1016/0191-8141(93)90158-7

Srivastava, D. C., Lisle, R. J., Imran, M., & Kandpal, R. (1998). The kink-band triangle: A triangular plot for paleostress analysis from kink-bands. *Journal of Structural Geology*, *20*, 1579–1586. https://doi.org/10.1016/S0191-8141(98)00051-0

Srivastava, D. C., Lisle, R. J., Imran, M., & Kandpal, R. (1999). A new approach for paleostress analysis from kink bands: Application of fault-slip methods. *Journal of Geology*, *107*, 165–176. https://doi.org/10.1086/314340

Stickle, A. M., & Schultz, P. H. (2013). Investigating pressure magnitudes at depth for oblique impacts into layered targets: Applications to terrestrial impacts in sedimentary targets. *Meteoritics and Planetary Science*, *48*, 1638–1650. https://doi.org/10.1111/maps.12152

Winkler, R., Luther, R., Poelchau, M. H., Wünnemann, K., & Kenkmann, T. (2018). Subsurface deformation of experimental hypervelocity impacts in quartzite and marble targets. *Meteoritics and Planetary Science*, *23*, 1–23. https://doi.org/10.1111/maps.13080

Wood, C.A., Head, J.W., Cintala, M.J., 1978. Interior morphology of fresh Martian craters-The effects of target characteristics, in: Lunar and Planetary Science Conference Proceedings. pp. 3691–3709.

Xia, K., & Ahrens, T. J. (2001). Impact induced damage beneath craters. *Geophysical Research Letters*, *28*, 3525–3527. https://doi.org/10.1029/2001GL013001

Yokoyama, E., Trindade, R. I. F., Lana, C., Filho, C. R. S., Baratoux, D., Marangoni, Y. R., & Tohver, E. (2012). Magnetic fabric of Araguainha complex impact structure (Central Brazil): Implications for deformation mechanisms and central uplift formation. *Earth and Planetary Science Letters*, *331–332*, 347–359. https://doi.org/10.1016/j.epsl.2012.01.005

References From the Supporting Information

Ahrens, T. J., & Johnson, M. L. (1995). Shock wave data for rocks. Mineral physics and crystallography. In T. J. Ahrens (Ed.), *A handbook of physical constants* (Vol. 3, pp. 35–44). Washington, DC: American Geophysical Union.

Hoerth, T., Schäfer, F., Hupfer, J., Millon, O., & Wickert, M. (2015). Momentum transfer in hypervelocity impact experiments on rock targets. *Procedia Engineering*, *103*, 197–204.

Moore, H. J., Lugn, R. V., & Gault, D. E. (1962). Experimental hypervelocity impact craters in rock. *Proceedings of the 5th Symposium on Hypervelocity Impact*, *1*(Pt 2), 625–643.

Perret, W. R., & Bass, R. C. (1975). Free-field ground motion induced by underground explosions (No. SAND-74-0252). Sandia Labs., Albuquerque, N. Mex.(USA).

Smrekar, S., Cintala, M. J., & Hörz, F. (1986). Small-scale impacts into rock: An evaluation of the effects of target temperature on experimental results. *Geophysical Research Letters*, *13*(8), 745–748.